Iranian Journal of Geophysics, Vol 20 No 3, 2026, Page 1 – 24 (Research Article)
DOI: 10.30499/ijg.2025.494060.1655

Revisiting wintertime budget of local finite-amplitude wave activity in the Northern Hemisphere storm tracks

Amin Fazl Kazemi[1], Alireza Mohebalhojeh[2*], Mohammad Mirzaei[3] and Farhang Ahmadi-Givi[2]

[1] *Ph.D., Student of Meteorology, Institute of Geophysics, University of Tehran, Tehran, Iran*
[2] *Professor, Institute of Geophysics, University of Tehran, Tehran, Iran*
[3] *Associate Professor, Institute of Geophysics, University of Tehran, Tehran, Iran*

(Received: 15 December 2024, Accepted: 19 April 2025)

Abstract

The climatological distribution of the local finite-amplitude wave activity (LWA) and its three-dimensional flux components are studied for boreal winter (December to February) using the JRA-55 reanalysis dataset for the period 1979–2023. The methods for extracting the Lagrangian reference state of quasigeostrophic potential vorticity and obtaining density-weighted vertical average are modified to expand the domain of validity to include highland and low-latitude regions of the Northern Hemisphere. A novel summarization method is also proposed to extract spatial scale and identify the local dominant balances within the LWA budget terms. Additionally, variations in the LWA flux divergence components are examined for the layers representing the upper, middle and lower troposphere, as well as for the vertical profiles in the selected horizontal areas with the storm tracks. The differences observed in the distribution of LWA and its flux divergence, compared to previous studies, are qualitatively consistent with the available Eulerian diagnostics for small-amplitude disturbances. The finite-amplitude Lagrangian formulation makes it possible to provide more accurate estimates of the nonconservative source/sink processes. These estimates are revised using the diagnostics related to the geostrophic states, based on a formal quasigeostrophic inversion. The main dominant balance observed for the column-averaged budget is between the near-surface baroclinicity, which generates the vertical flux of LWA, and the nonconservative processes. The results show that, while the North Atlantic and North Pacific storm tracks exhibit similar patterns with regard to the source of LWA, they behave quite differently at the regional scale in terms of the balance between the LWA budget terms.

Keywords: Local finite-amplitude wave activity, lagrangian reference states, quasigeostrophic potential vorticity, wave activity flux divergence, baroclinic eddy

---

[*] Corresponding author: amoheb@ut.ac.ir

1 Introduction

The wave activity conservation law in its generalized form (Andrews et al., 1987) provides a potent diagnostic framework to study the large-scale processes that shape the distribution of eddies in the atmosphere. The foundation for such conservation law rests on the material conservation of a form of potential vorticity and potential temperature in the absence of nonconservative processes. The formulations for wave activity, which are directly applicable to the vast reanalysis data available for both the climatological and case studies, have been particularly appealing. The purely Eulerian formulations, which are formally valid only for small-amplitude disturbances (Plumb, 1986; Esler and Haynes, 1999; Takaya and Nakamura, 2001), suffer from a problem with applicability for wave-activity density in regions where meridional potential vorticity gradient of the mean state vanishes or becomes negative. By construction, no such problems are present in the group of formulations of wave activity that exploit Lagrangian information available in potential vorticity to ensure validity for finite-amplitude disturbances (Haynes, 1988; Nakamura and Zhu, 2010; Methven and Berrisford, 2015). In the latter group, the formulation of Nakamura and Zhu (2010) and its extension to include zonally-varying effects (Huang and Nakamura, 2016) combine conceptual simplicity with the theoretical advantage of preserving a form of local nonacceleration theorem.

Since its introduction, the local finite-amplitude wave activity (LWA) of Huang and Nakamura (2016) has been used in several studies, including for a new interpretation and model of atmospheric blocking (Nakamura and Huang, 2018), the mid-winter suppression of the North Pacific storm track (Zhao and Liang, 2019), mountain effects in upstream areas (Sacha et al., 2021), the temporal evolution of early summer cut-off lows in north-eastern Asia (Nie et al., 2023), extreme weather events (Chen et al., 2015; Neal et al., 2022), Ural blocking dynamics (Wang et al., 2021), variability and pattern similarities of blockings at the Euro–Atlantic sector (Teubler et al., 2023). The first attempt to determine the dynamical processes controlling the distribution of LWA was made by Huang and Nakamura (2017), hereafter referred to as HN17 for brevity. Having established the connection with zonal wind, HN17 provided the first estimates of the column-wise budget of LWA for the Northern Hemisphere during boreal winter (December to February, or DJF for brevity). They noted certain differences between the climatological seasonal mean and the synoptic-scale time variability, especially regarding the importance of the near-surface vertical flux of wave activity. A dominant balance was also reported between the near-surface vertical flux and the zonal flux divergence, particularly over the North Atlantic storm track. The discrepancy in the position of maximum horizontal flux divergence over the major storm tracks between the LWA diagnostics and those of the small-amplitude formulation of Esler and Haynes (1999) for the upper troposphere, as reported in Rezaeian et al. (2016), motivated us to re-examine the LWA diagnostics over the Northern Hemisphere. Earlier works on the eddy kinetic energy diagnostics (Chang et al., 2002) and the wave-activity diagnostics (Nakamura and Solomon, 2010; Rezaeian et al., 2016; Esmaeli et al., 2022) have shown that the major storm tracks of the Northern Hemisphere can be identified using a pair of positive and negative regions of horizontal flux divergence of a quantity representing the magnitude of eddies. This provides a simple yet useful view of storm tracks in terms of Rossby wave propagation from an upstream emitter region to a downstream receiver region. Reconciling the early LWA diagnostics of HN17 with this perspective, however, leads to a picture of the storm tracks where the emitter region is located far downstream. One may speculate that this apparent shift is due to the higher-order effects not accounted for in the small-amplitude formulations. That is, the signature of strong Rossby-wave events such as blocking highs may lead to such changes in the picture. The extent to which the finite- and small-amplitude theories agree is a central question that remains worth studying. The other motivation for our study comes from the power of the finite-amplitude formulations in giving us more information on the nature of nonconservative processes that shape the distribution of eddies. This removes the inherent ambiguity due to the impact of nonlinear large-amplitude disturbances, when small-amplitude Eulerian forms of wave activity are used.

The paper is organized as follows. The mathematical formulation and problem setup are discussed in section 2. Also, in this section the revision made in the computation of density-weighted vertical integrals involved is described. In section 3, the data and methods are introduced. In section 4, the results for each term in the budget equation is discussed in detail. Emphasize here is on the role of nonconservative processes. To investigate differences in characteristics between different storm-track regions, the results of budget terms are summarized in a novel map that depicts the dominant balance within the budget. This is complemented by investigation of the vertical variation of flux divergence components as well as estimates for the nonconservative processes in the troposphere. Finally, the concluding remarks are presented in section 5.

2 Mathematical formulation

Following Nakamura and Solomon (2010), the quasigeostrophic potential vorticity, hereafter PV, on pseudo-height logarithm of pressure z is written in the form of:

$$q = f + \frac{1}{a\cos\varphi}\left(\frac{\partial v}{\partial\lambda} - \frac{\partial(u\cos\varphi)}{\partial\varphi}\right) + \frac{f}{\rho_0}\frac{\partial}{\partial z}\left[\frac{\rho_0(\theta-\tilde{\theta})}{\partial\tilde{\theta}/\partial z}\right], \qquad (1)$$

where q denotes the PV, u and v are respectively the zonal and meridional velocities, a is the earth's radius taken to be uniform and equal to 6378 km, φ is latitude, λ is longitude, $f = 2\Omega\mu$ is the Coriolis parameter with Ω the earth's rotation rate and $\mu = \sin\varphi$, ρ_0 is the reference density, and $\tilde{\theta}$ is taken to be the spatial average of the potential temperature θ on pressure levels over the Northern Hemisphere. It should be noted that, by using Eq. (1), the formal asymptotic validity of the quasigeostrophic model is abandoned in favor of extending the domain of applicability to low latitudes.

Now for a given Q contour of PV, the so-called equivalent latitude φ_{REF} is sought such that the area enclosed by the eddy north of $Q(\varphi_{\mathrm{REF}}, z, t)$ contour is equal to the area enclosed to its south. For the schematic PV contour shown in Fig. 1, this means that the area shaded light gray is equal to the area shaded dark gray in the lower panel. The PV over the area shaded dark gray is greater than Q whose subset situated south of the equivalent latitude defines the cyclonic component of LWA. Similarly, PV over the area shaded light gray is lower than Q whose subset situated north of the equivalent latitude defines the anticyclonic LWA component.

The two components of LWA are positive by definition except on the unrealistic condition where the Q contour is purely zonal, which leads to zero LWA. The LWA components are calculated

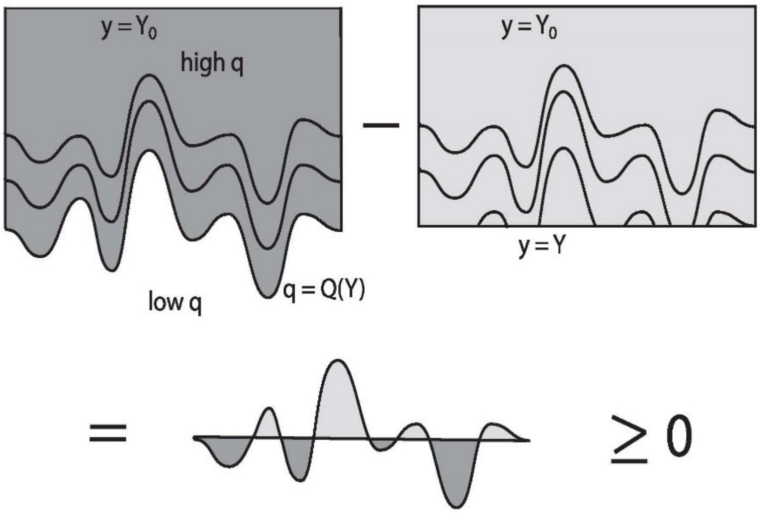

Figure 1. A schematic representation of the equivalent latitude and the corresponding partitioning of areas, adapted from Nakamura and Zhu (2010).

using the following surface integrals:

$$LWA_{\text{cyclonic}}(\lambda,\varphi,\varphi_{\text{REF}},z,t) = \frac{1}{\cos\varphi}\int_{q>Q;0\le\varphi'<\varphi_{\text{REF}}} \left(q(\lambda,\varphi',z,t) - Q(\varphi_{\text{REF}},z,t)\right) a\cos\varphi' \mathrm{d}\varphi' ,$$

$$LWA_{\text{anticyclonic}}(\lambda,\varphi,\varphi_{\text{REF}},z,t) = \frac{1}{\cos\varphi}\int_{q<Q;\pi/2\ge\varphi'>\varphi_{\text{REF}}} \left(Q(\varphi_{\text{REF}},z,t) - q(\lambda,\varphi',z,t)\right) a\cos\varphi' \mathrm{d}\varphi' \cdot \tag{2}$$

With a slight modification, the method is used to compute the reference state zonal wind $u_{\text{REF}}(\varphi_{\text{REF}},z,t)$, and the reference state potential temperature $\theta_{\text{REF}}(\varphi_{\text{REF}},z,t)$ is the same as that described in the complementary materials of Neal et al. (2022). The eddy part of the horizontal wind components $(u',v')|_{\lambda,\varphi,\varphi_{\text{REF}},z,t} = \left(u(\lambda,\varphi,z,t) - u_{\text{REF}}(\varphi_{\text{REF}},z,t), v(\lambda,\varphi,z,t)\right)$ and the eddy part of the potential temperature $\theta'|_{\lambda,\varphi,\varphi_{\text{REF}},z,t} = \theta(\lambda,\varphi,z,t) - \theta_{\text{REF}}(\varphi_{\text{REF}},z,t)$ are then used. The total LWA is defined by:

$$\tilde{A}^\star(\lambda,\varphi,\varphi_{\text{REF}},z,t) = LWA(\lambda,\varphi,\varphi_{\text{REF}},z,t) = LWA_{\text{cyclonic}} + LWA_{\text{antiyclonic}} \cdot \tag{3}$$

Defining the 3-dimensional gradient operator $\nabla_3 = \left(\frac{\partial}{a\cos\varphi_{\text{REF}}\partial\lambda}, \frac{\partial}{a\,\partial\varphi'}, \frac{\partial}{\partial z}\right)$, the exact conservation law is written in the form of:

$$\frac{\partial \tilde{A}^\star\cos\varphi\, e^{-z/H}}{\partial t} + \nabla_3\cdot e^{-z/H}\mathbf{F} = e^{-z/H}S , \tag{4}$$

where S denotes the nonconservative effects, H is the pressure scale height and $e^{-z/H}$ plays the role of density. The LWA flux is then decomposed into the radiative (generalized Eliassen–Palm) and advective components as $\mathbf{F}(\lambda,\varphi_{\text{REF}},z,t) = \mathbf{F}_{\text{EP}}(\lambda,\varphi_{\text{REF}},z,t) + \mathbf{F}_{\text{ADV}}(\lambda,\varphi_{\text{REF}},z,t)$. A further decomposition involves the zonal advective LWA flux, which is split into the linear part

$$\mathbf{F}_{\text{ADV,linear}} = \text{Linear Advection} = O(\alpha^2) = \left(u_{\text{REF}}(\varphi_{\text{REF}},z,t)\cos\varphi\tilde{A}^\star(\lambda,\varphi,\varphi_{\text{REF}},z,t) ,0 ,0\right) , \tag{5}$$

where α denotes the wave amplitude, and the nonlinear part corresponding to the Stokes drift by $\mathbf{F}_{\text{Nonlinear}} = O(\alpha^3) = (F^{\lambda}_{\text{ADV},N\text{onlinear}}, 0,0)$ with

$$F^{\lambda}_{\text{ADV},N\text{onlinear}} = \int_{q>Q,0\le\varphi<\varphi_{\text{REF}}} \left(u(\lambda,\varphi,z,t) - u_{\text{REF}}(\varphi_{\text{REF}},z,t)\right)\left(q(\lambda,\varphi,z,t) - Q(\varphi_{\text{REF}},z,t)\right) a\cos\varphi d\varphi + \int_{q<Q,\pi/2\ge\varphi\ge\varphi_{\text{REF}}} \left(u(\lambda,\varphi,z,t) -\right.$$

$$u_{\mathrm{REF}}(\varphi_{\mathrm{REF}}, z, t)\big)\big(Q(\varphi_{\mathrm{REF}}, z, t) - q(\lambda, \varphi, z, t)\big)\, a \cos\varphi d\varphi. \tag{6}$$

The radiative Eliassen–Palm flux $\mathbf{F}_{\mathrm{EP}}$ is given by:

$$\mathbf{F}_{\mathrm{EP}} = \cos\varphi \left(\frac{v'^2 - u'^2}{2} - \frac{R\, e^{-\kappa z/H}}{2H} \frac{\theta'^2}{\partial\tilde{\theta}/\partial z}, -u'v', \frac{f v'\theta'}{\partial\tilde{\theta}/\partial z}\right) \tag{7}$$

Here, R is the gas constant for dry air, and $\kappa = R/c_p$, where c_p is the specific heat of dry air at constant pressure. Using the foregoing relations, we will be able to perform the calculation of related flux components.

For PV in the form of Eq. (1), the hemispherically area averaged potential temperature is used. The extreme PV values are set to Q_{REF} at the latitudinal boundaries (i.e., the two poles in the global approach, or the equator and each pole separately in the hemispheric approach). The main requirement for the distribution of Q_{REF} is its monotonic increase with latitude, regardless of the details of the two-dimensional distribution of PV at each vertical level. Details of the computational method designed to extract Q_{REF} is given in Appendix A.

2-1 Density-weighted vertical averaging revised

To obtain vertical average, which will be denoted by angle brackets, use is made of the reference density of each level. The vertical average from the sea surface up to the model top (48 km here) can be displayed by $\langle \ldots \rangle = \frac{\int_0^\infty (\ldots) e^{-z/H}\, dz}{\int_0^\infty e^{-z/H}\, dz}$, where $H = \int_0^\infty e^{-z/H}\, dz$ in the denominator denotes the pressure scale height considered to be equal to 7 km. The discretized form of this formula can be determined as $\langle (\ldots) \rangle \approx \frac{\sum_{k=2}^{nz} (\ldots)_k e^{-z_k/H}\, dz}{\sum_{k=2}^{nz} e^{-z_k/H}\, dz}$. Using nz=97 and dz=500 m, the denominator is approximately equal to 6745 m. Even though the above formula is readily applicable for the vast oceanic areas as the major study target of storm tracks, its direct implementation over the land, particularly highly elevated regions, will result in using grid points below the earth's surface with high density weights, which may adversely affect the results. An immediate solution is to confine the study to open sea and almost low-level flat areas; however, the high vertical resolution leads to coverage of a large portion of land areas. To circumvent this limitation, here the density-weighted vertical averaging is modified by:

$$\langle \ldots \rangle \equiv \frac{\int_{z_{\mathrm{bot}}}^{\infty} (\ldots) e^{-z/H}\, dz}{\hat{H}}, \tag{8}$$

where z_{bot} is the surface elevation plus one km to approximately take into account the planetary boundary layer, and $\hat{H} = \int_{z_{\mathrm{bot}}}^{\infty} e^{-z/H}\, dz$. This can be carried out by taking the vertical differential consistent with the surface topography, while using the same pseudo-height levels as:

$$dz_{\mathrm{modified}}\big|_{i,j,k} = \begin{cases} 0\ ;\ z_{\mathrm{bot}}\big|_{i,j} \leq\ z_k\ , \\ z_k - z_{\mathrm{bot}}\big|_{i,j}\ ; z_{k-1} \leq z_{\mathrm{bot}}\big|_{i,j} \leq z_k. \\ dz\ ;\ otherwise\ \cdot \end{cases}$$

Finally, the vertical average of each variable can be obtained by the discretized relation:

$$\langle (\ldots) \rangle\big|_{i,j} \approx \frac{\sum_{k=2}^{nz} (\ldots)_{i,j,k} e^{-z_k/H}\, dz_{\mathrm{modified}}\big|_{i,j,k}}{\hat{\hat{H}}}, \tag{9}$$

where $\hat{\hat{H}} = \sum_{k=2}^{nz} e^{-z_k/H} dz_{\mathrm{modified}}\big|_{i,j,k}$ corresponds to the discrete form of $\hat{H}$, which varies with surface topography, ranging from 3071 m over the highest point in the reanalysis dataset used to approximately 6280 km over open oceans. Applying the above averaging operator, the conservation relation in its density-weighted vertical average is written as:

$$\frac{\partial \langle A \rangle \cos\varphi}{\partial t} = -\frac{1}{a\cos\varphi} \left\langle \frac{\partial F^{\lambda}}{\partial \lambda} \right\rangle + \frac{1}{a\cos\varphi} \left\langle \frac{\partial u'v' \cos^2(\varphi + \varphi')}{\partial \varphi} \right\rangle + \frac{1}{\hat{H}} F_z\, e^{-z/H}\Big|_{z_{\mathrm{bot}}} + \langle S \rangle\ \cdot \tag{10}$$

For ease of reference, a name convention is established here in order to refer to the terms involved in the budget of LWA. For this, the first through fourth terms in the right-hand side of Eq. (10) are referred to as CZF, CMF, SF, and SS, representing, respectively, the convergence of zonal flux, convergence of meridional flux, surface flux, and source/sink. The sum of CZF and CMF is referred to as CHF, representing the convergence of horizontal flux.

3 Data and methodology

The JRA-55 Japanese reanalysis (Kobayashi et al., 2015) is used to calculate the diagnostics. This dataset is accessible in the two editions on pressure and isentropic levels. We used the version coarsened to the regular 1.25° latitude–longitude grid defined on the major 6-hourly synoptic times. The dataset is available from 1958 when the global radiosonde data network was first established. At the time of its publication, it was considered as the first reanalysis dataset spanning 50 years as well as first operational long-term use of four-dimensional variational data assimilation.

To estimate LWA and its flux components, the reanalysis data were interpolated to the equidistant logarithmic-pressure pseudo-height levels at 500 m interval and used with 12-hour time steps (00 UTC). The wintertime months (December to February) between 1978–79 and 2022–23 are studied in this paper. All the terms contributing to the LWA conservation relation are computed at each time step and then averaged vertically, over each season and the entire duration of the climatological period in this study. The time-averaged effect of nonconservative processes over the climatological period is estimated by the time-averaged divergence of three-dimensional flux of LWA, which is equal to - (CHF+SF). In the Eulerian formulations that are strictly valid only for small amplitude waves, the corresponding estimate for nonconservative processes is contaminated by the nonlinear effects. To make this point, a comparison is also given by presenting results for the Eulerian small-amplitude formulation of Esler and Haynes (1999), a brief description of which is given in Appendix B. In addition to the usual diagnostics, a novel summarization composite is produced showing the local dominant balance in the wintertime budget of LWA.

4 Results for wave-activity diagnostics

4-1 Local wave activity

The first diagnostic presented in Fig. 2 is $\langle A\cos\varphi\rangle$, decomposed to its transient and stationary components, along with the climatological mean zonal wind. The method used to separate the transient (Fig. 2a) and stationary (Fig. 2b) components is the same as HN17, namely calculating the stationary component of LWA based on the seasonally-averaged wind and potential temperature and subtracting it from the seasonally-averaged LWA to estimate the transient component of LWA. To encompass the complete range of transients possible, no temporal filtering is applied. The transient LWA can be compared with the corresponding result in Fig. 2c of HN17, as well as that of the small-amplitude formulation of Plumb (1986) presented in Fig. 2d of HN17. It should be noted that the HN17 results were obtained using ERA-Interim reanalysis data at 6-hourly interval, 1.5° spatial resolution and 1 km vertical spacing on log-pressure pseudo-height levels, covering the 39-year period from 1979 to 2017. When comparing our results with those in HN17, therefore, one should take into account the finer horizontal resolution and vertical spacing, and the longer time period in our study.

There are main differences to note in the transient component of LWA, especially over the North Atlantic in this study and HN17. The large gap in LWA between the west and east of the Atlantic in HN17 is in sharp contrast with the continuous zonal band of activity in Fig. 2a. There is only a faint sign of the southward intrusion of LWA over the central North Atlantic in HN17. In this aspect, the present results for the transient LWA are more consistent with those of Plumb (1986). Across the Pacific, both our results and those of HN17 show that LWA is zonally stretched north of the subtropical jet. There is, however, a distinct separation between the Pacific and Atlantic storm tracks over the east of the North Pacific and west of the continental US in HN17. In contrast, no such distinct separation is observed in activity between the two storm tracks for the total LWA, i.e., the sum of transient and stationary components in Fig. 2c. A rather similar feature can be seen in the corresponding result shown in Fig. 2 of Wang et al. (2021) and Fig. 2 of Valva and Nakamura (2021). Over Europe, Fig. 2a points to the existence of large transient LWA over a region which is substantially displaced from the jet core. This feature is consistent with the non-acceleration theorem in the sense that the maxima of LWA tend to occur over the minima of the climatological mean flow, which forms the background environment for the development and propagation of the eddies. This provides the theoretical basis to understand differences noted for the distribution of LWA and the related diagnostics between the North Atlantic and North Pacific storm tracks.

Unlike the transient component, our results agree well with those in HN17 (see Fig. 2b) for the stationary component. The centers of strong stationary LWA, upstream of the North Pacific storm track at the western coast of the Sea of Japan, a region between Britain and Scandinavian Peninsula, as well as the Hudson Bay at the east coast of the US and upstream of the North Atlantic storm track are the features to note in Fig. 2b.

To gain further insight into the distribution of LWA, Figs. 3a and 3b show the transient cyclonic and anticyclonic LWA components, which can be interpreted as the net effect of finite-amplitude travelling troughs and ridges, respectively. A very strong anticyclonic LWA center in the eastern North Atlantic and western Europe, shown in Fig. 3b, is a

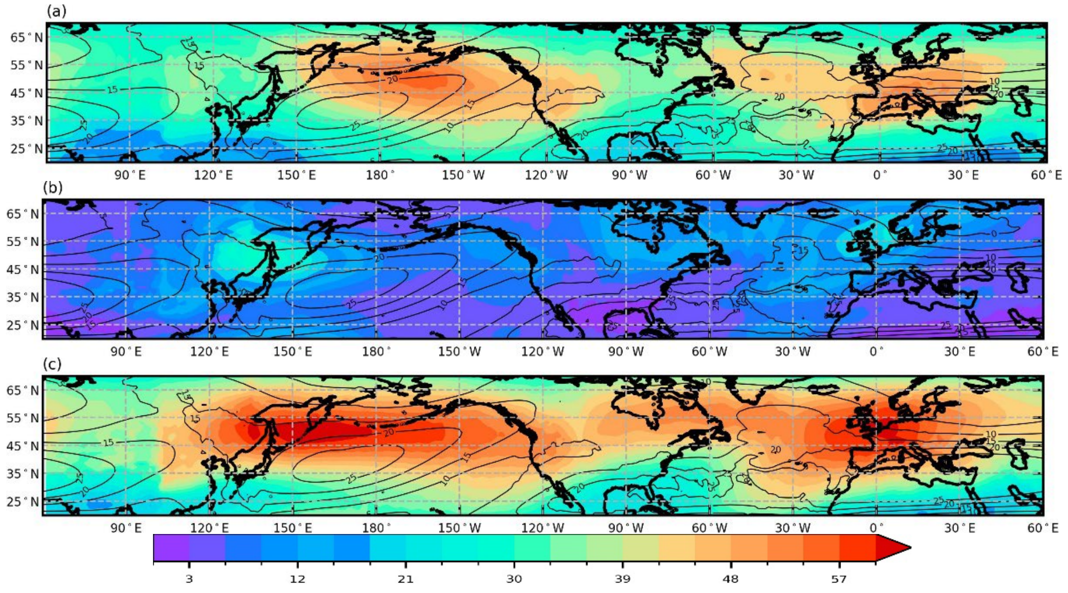

Figure 2. The vertically-averaged LWA (shaded with units of m/s) due to (a) transient, (b) stationary, and (c) transient plus stationary waves in boreal winter (DJF) from 1979 to 2023. Contours show the climatological mean zonal wind with interval of 5m/s for the same period.

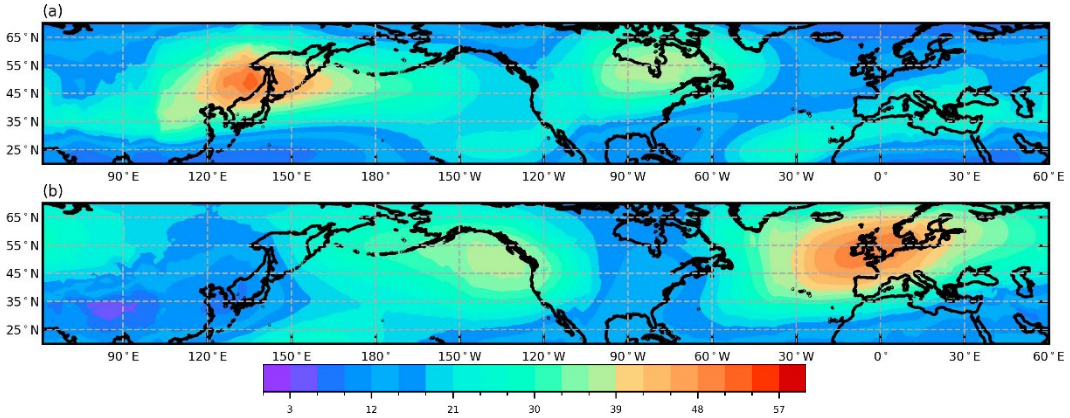

Figure 3. The vertically averaged (a) cyclonic and (b) anticyclonic contributions to the local finite-amplitude wave activity (in units of m/s) due to transient waves in the Northern Hemisphere winter (December to February) from 1979 to 2023.

manifest of extended intrusion and breaking of waves at the downstream end of the North Atlantic storm track. It is also coincident with a main region of the formation of blocking high in the Euro-Atlantic sector (Azarm et al., 2023). At the same time, the coincidence with the maximum stationary LWA (Fig. 2b) points to the dominance of this center of anticyclonic LWA. Similarly, there is a region of anticyclonic LWA over the northeast of the North Pacific, though much weaker than the North Atlantic counterpart. Note that in the same region in the North Pacific, the stationary LWA is also weaker than the North Atlantic counterpart. Unlike the case for the anticyclonic wave activity, the cyclonic LWA maximizes upstream of the two major storm tracks comprising a strong center over the northeast of Asia and a weaker center over the northeast of Canada (Fig. 3a). The signature of the latter two centers of cyclonic LWA can also be seen in the stationary component (Fig. 2b).

4-2 The near-surface vertical flux

To understand the possible balances that determine the distribution of LWA, we start by presenting the near-surface vertical flux of LWA, i.e., the SF term in Eq. (10), which with an opposite sign is equivalent to the vertical divergence of vertical component of LWA flux and represents the meridional potential temperature flux near the surface (Fig. 4). There is a good degree of agreement between Fig. 4a and the corresponding result in HN17, with the difference being a more distributed flux across the two oceanic basins in our results. Decomposing SF into the stationary and transient components in the same way as that carried out for LWA, one can see a significant contribution by the stationary component (Fig. 4b), especially over the east of the North Pacific and North Atlantic. The latter two sources of LWA over the east of the oceans play a major role in maintaining wave activity. Over the North Atlantic, the transient low-level heat flux (Fig. 4c) seems to follow the core of storm activity in a southwest–northeast direction (Scherrmann et al., 2023).

4-3 The horizontal divergence of wave activity flux

The second quantity to consider in the maintenance of LWA is the CZF term in Eq. (10), which is decomposed into the radiative and advective parts. The radiative part is a generalization of the Eliassen–Palm flux for the zonal direction, and the advective part is further decomposed to a linear part and a third-order in amplitude nonlinear part corresponding to the Stokes drift. CZF is thought to be an essential part of blocking formation and suppression of synoptic-scale wave transience (Nakamura and Huang, 2018). The radiative zonal flux itself includes a dynamic part involving relative difference between eddy wind variances and a thermodynamic part involving the ratio of squared eddy potential temperature variance to its basic state stratification.

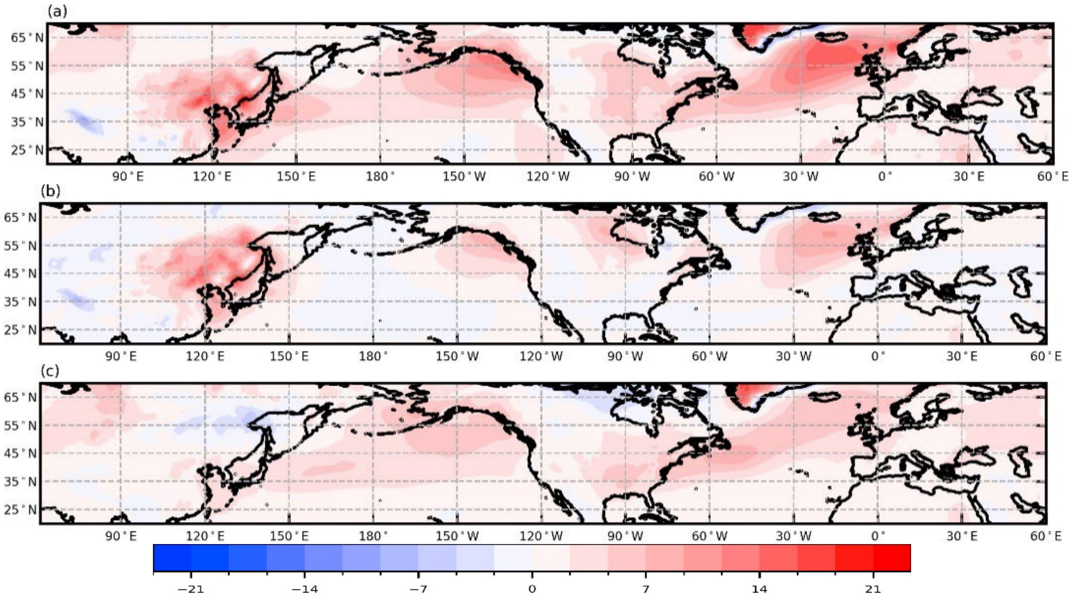

Figure 4. The near-surface vertical flux of wave activity, represented by the SF term in Eq. (10), averaged over boreal winters (DJF) from 1979 to 2023. The results are shown as: (a) total, (b) stationary and (c) transient wave effects according to the method proposed by HN17. The units are $10^{-5}\ m/s^2$.

The amplitude of propagating waves decreases when they continue their excursion over land, leading to the generation of fronts on the western coasts of the continents with an opposite effect over the eastern coasts. The other important effect is related to the intensification of waves due to local orography and mountain ranges in Russia and northern China, which are located upstream of the North Pacific storm track. These features intensify the waves entering into the area and play a significant role in their life cycles (for the analogous situation in the North Atlantic storm track, see Scherrmann et al., 2023).

Referring to Fig. 5a for the total zonal LWA flux convergence, the major difference between the position and spatial extent of the wave emission region of negative CZF, particularly over the North Atlantic, in this study and those in Fig. 3a of HN17 is directly related to difference in the LWA itself. The coastal frontal regions, especially over the western Scandinavian Peninsula, still exist here. The same is true for the southeast–northwest oriented mountain ranges, such as the Rockies. Also, the net oceanic wave emission regions of negative CZF are formed as a strip with the southwest–northeast orientation over the west of the North Atlantic and North Pacific oceans, though with much weaker values compared to results shown in Fig. 3a of HN17. Together with the wave reception regions of positive CHF at their downstream, the foregoing wave emission regions constitute the building blocks of the two oceanic storm tracks.

The eddy meridional momentum flux gives us information on Rossby wave breaking and momentum deposition by eddies into the mean flow. The climatological mean vertically-averaged wintertime meridional LWA flux convergence, CMF in Eq. (10), is illustrated in Fig. 5b. The last proposed modifications of Neal et al. (2022) are included in calculating the CMF term, which matches well with the corresponding result shown in Fig. 3b of HN17. Compared to the total CZF (Fig. 5a), the southwest–northeast oriented region of negative CMF over the North Atlantic is located directly at the southeast or downstream of the region of negative CZF and helps extend the wave emission region. The net result, i.e., the sum of CZF and CMF, is shown in Fig. 5c as CHF or the convergence of horizontal flux. The constructive superposition of the zonal and meridional contributions extends to subtropical regions of the Northern Hemisphere and the northwestern coast of Africa. CZF becomes dominant over most land areas, except for some parts of central Siberia, where negative CMF values preferentially reinforce wave emission.

The two components of CHF illustrate a destructive superposition over the western Pacific between 20°N and 45°N, which is extended to the middle and eastern Pacific Ocean (Fig. 5c). A main region of negative CHF is centered around 120°E and 45°N, which can be considered as the main wave emission region of the Pacific storm track. The relatively large contribution of the meridional momentum flux indicates early wave breaking at the entrance to the North Pacific storm track, related to the mountain effect from upstream, particularly the zonally-extended Himalayas. Over the North Atlantic, extending downstream over Europe and the Mediterranean, there is also some degree of destructive superposition between the CZF and CMF, leading to weaker signature for CHF. This has significant consequences for the column-wise wave activity budget as discussed below.

As argued by HN17, the residual of the LWA budget conservation relation can be directly interpreted as the nonconservative source/sink, the SS term or $\langle S \rangle$ in Eq. (10), which is mainly the result of diabatic heating at the lower troposphere and irreversible potential vorticity mixing at the upper troposphere. This can be verified if vertical cross-sections over the preferred regions of the three-dimensional nonconservative source/sink are produced (not shown here). Over the oceanic basins, the results shown in Fig. 5d are in overall agreement with those in Fig. 3d of HN17 on the dominance of negative values, meaning the dissipative nature of $\langle S \rangle$. At the same time, there are pockets of small positive $\langle S \rangle$ over the mid-Atlantic and Pacific, which can be attributed to the source effect of diabatic heating in amplifying wave activity. The other notable regions of positive $\langle S \rangle$ are those over the central Mediterranean and downstream of the mountain ranges of Northern Hemisphere over the continents.

4-4 The dominant balances

Having presented the terms contributing to the conservation law for LWA, the question then arises on which terms play the dominant role in the budget of LWA in the climatological mean. To this end, a map (Fig. 6) has been provided for partitioning the domain based on the two main terms that determine the local balance in the budget for each grid point of the domain. In HN17, for the climatological mean over the Northern Hemisphere storm tracks, the balance between the near-surface vertical flux (positive SF) and the zonal flux divergence (negative CZF) is recognized as dominant. What presented in Fig. 6, however, points to a more complex picture. A variety of balances can be distinguished even when restricting

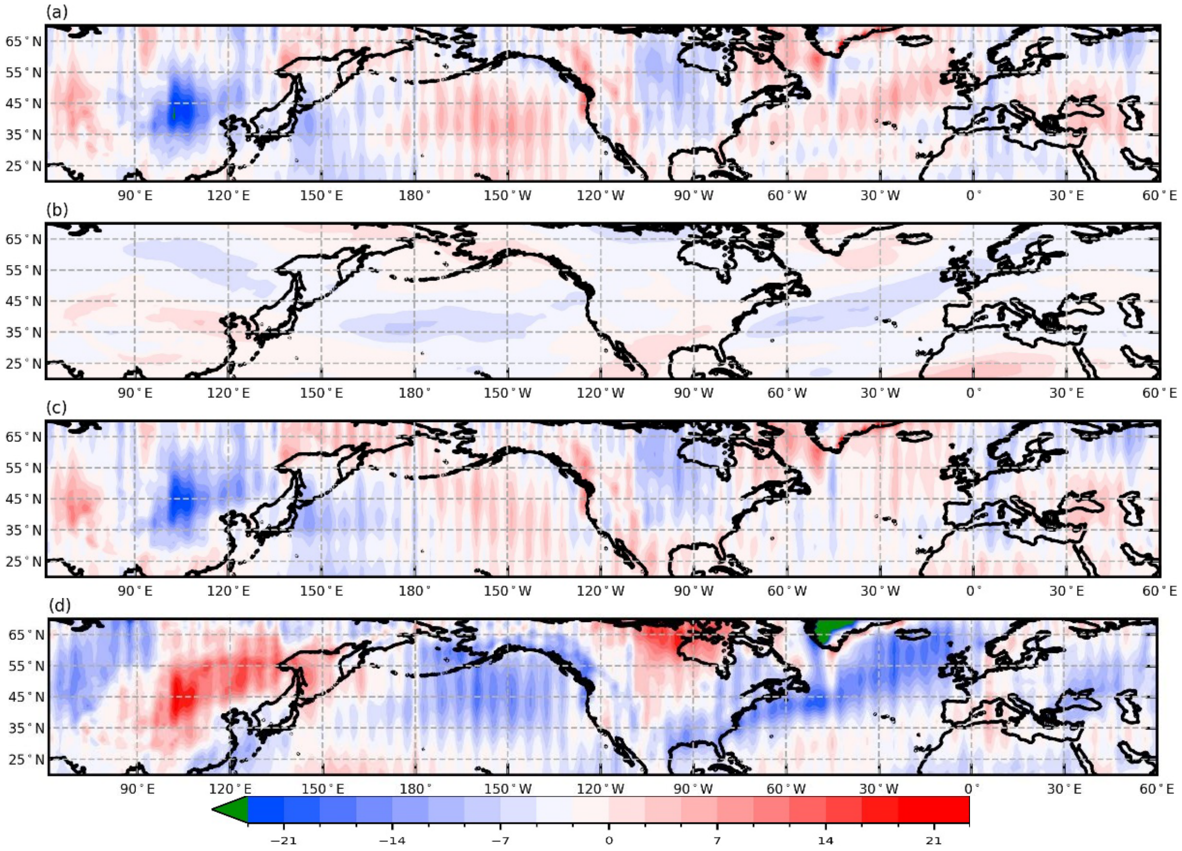

Figure 5. The vertically averaged (a) CZF, (b) CMF, and (c) CHF, which is averaged over boreal winters (DJF) for the period 1979–2023. (d) The estimate for the climatological mean of nonconservative effect or SS term in Eq. (10). The units are $10^{-5}\ \mathrm{m/s^2}$.

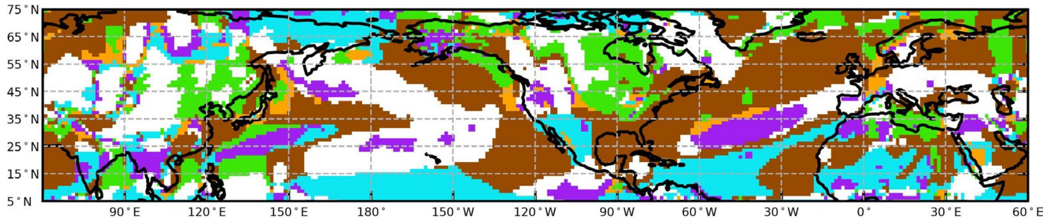

Figure 6. The dominant local balance between the LWA budget terms for the average results of boreal winters (DJF) over the period 1979–2023. The dominant balances are between the following terms: purple represents the balance between zonal and meridional flux divergence; light green represents the balance between near-surface vertical flux and zonal flux divergence; white represents the balance between zonal flux divergence and nonconservative processes; light blue represents the balance between meridional flux divergence and nonconservative processes; brown represents the balance between near-surface vertical flux and nonconservative processes; and orange represents the balance between near-surface vertical flux and meridional flux divergence. To remove small-scale noise, a low-pass spectral filter with the cutoff zonal wavenumber 30 has been applied to the advective zonal flux.

attention to the main oceanic basins. There are regions of balance between SF and SS downstream and upstream of the two main storm tracks. Over the continents, the main balancing terms are CZF and SS. In the low latitudes of the two oceanic basins, CMF and SS have the dominant role, meaning the interplay between the meridional wave propagation/breaking and the nonconservative processes. There are also regions of balance between CZF and CMF, especially as southwest–northeast stretched bands over the Pacific and Atlantic.

4-5 The vertical distribution of diagnostics in the troposphere

Given the time-averaged wave-activity budget for the vertical column covering the troposphere and stratosphere, the question remains on the vertical variations within the troposphere, where the storm tracks are mainly active. To address the question, the terms in the wave activity equations have been averaged over three layers: $[200,400]$ hPa, $[400,600]$ hPa, and $[600,800]$ hPa, representing the upper, middle and lower troposphere, respectively. The layer-averaged budget terms are compared with the corresponding results for the small-amplitude Eulerian formulation of Esler and Haynes (1999).

Fig. 7 presents the transient upper tropospheric layer-averaged zonal, meridional and vertical convergence of LWA flux for both Esler and Haynes (1999) and Huang and Nakamura (2016) formulations. For the zonal flux convergence, despite the contamination with noise of the small-amplitude Eulerian results, there is overall agreement between the two formulations regarding the main areas of flux convergence/divergence over the North Pacific and North Atlantic storm tracks (cf. Figs. 7a and 7d). The North Atlantic storm track is characterized by a southwest–northeast–oriented region of negative convergence (positive divergence) upstream, extending from the southeast of the US to Greenland and Iceland. This negative convergence area is paired with a southwest–northeast–oriented area of convergence stretched from the east of the North Atlantic to Europe and the Mediterranean. Most of Europe and the Mediterranean region lies within the domain of the North Atlantic storm track with no evidence of an independent Mediterranean storm track. For the North Pacific storm track, however, one can distinguish two zonally-oriented branches of flux divergence/convergence: the northern branch around 50°N associated with flux divergence across the North Pacific and flux convergence over the west of the US, and the southern branch around 25°N associated with flux divergence and convergence over the west and east of the North Pacific. Being weaker than its zonal counterpart, the meridional flux convergence exhibits a larger discrepancy between the Eulerian and Lagrangian formulations (Figs. 7b and 7e). For the vertical flux convergence (Figs. 7b and 7e), there are two main features to point out. First, in the absence of flux divergence areas, compared to the Lagrangian formulation, the flux

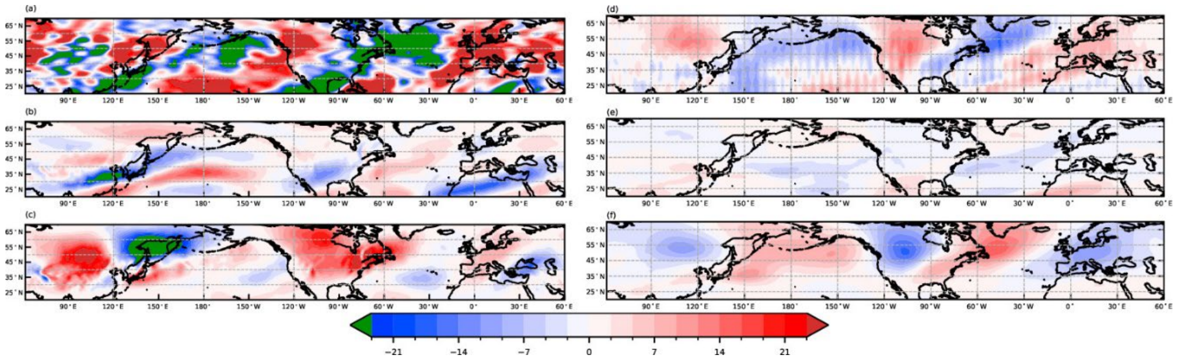

Figure 7. The transient upper-tropospheric layer-averaged convergence of (a,d) zonal, (b,e) meridional, and (c,f) vertical LWA flux averaged over boreal winters (DJF) from 1979 to 2023. Results shown are for the Esler and Haynes formulations (a–c), and the Huang and Nakumara formulations (d–f). The units are $10^{-5}\ \mathrm{m/s^2}$.

convergence areas are weaker over the North Pacific and North Atlantic storm tracks for the small-amplitude Eulerian formulation. Second, there is a remarkable cancellation between the zonal and vertical flux convergence in the Lagrangian formulation. As will be shown later, this finding points to the dominance of emission/reception over the source/sink of Rossby waves.

The vertically-averaged middle-tropospheric distribution of zonal, meridional and vertical convergence of the LWA flux for transient eddies is presented in Fig. 8. For the zonal flux convergence, the signatures of the North Pacific and North Atlantic storm tracks can be seen in both the Eulerian small-amplitude and Lagrangian finite-amplitude formulations. Relative to the upper troposphere, there is a marked westward shift in the position of the pairs of negative and positive flux convergence areas associated with the two oceanic storm tracks in such a way that the negative (positive) flux convergence areas in Figs. 8a and 8d tend to be located underneath the opposite-signed upper-tropospheric flux convergence areas. This leads to a large cancellation in the vertical column budget with consequences for the dominant balance (Fig. 6). In addition to the two prominent oceanic storm tracks, one can also distinguish areas of flux divergence over the western and central Mediterranean together with flux convergence over the eastern Mediterranean and the Red Sea region, which can be identified as the signature of the Mediterranean storm track. This feature is rather masked by small-scale noise in the Eulerian small-amplitude formulation. For the meridional flux convergence, no common feature is present between the results for the two formulations (Figs. 8b and 8e), while the two oceanic storm tracks are marked by a banded area of flux divergence, which is tilted in the southwest–northeast direction. For the vertical flux convergence, the result shown in Fig. 8c related to the Eulerian small-amplitude formulation is dominated by the flux convergence over the northwest of the Pacific storm track. In the Lagrangian finite-amplitude result (Fig. 8f), however, the flux divergence is the prominent feature over the northwest of the two oceanic storm tracks. This means that the latter two regions become wave-emission areas in the vertical direction, which is opposite that of the upper troposphere.

To complete the picture for the troposphere, the results for the lower troposphere are shown in Fig. 9. Due to the contamination with noise and also smaller amplitudes, the lower-tropospheric results are much less revealing for the zonal and meridional flux convergence. This is particularly the case for the Eulerian small-amplitude

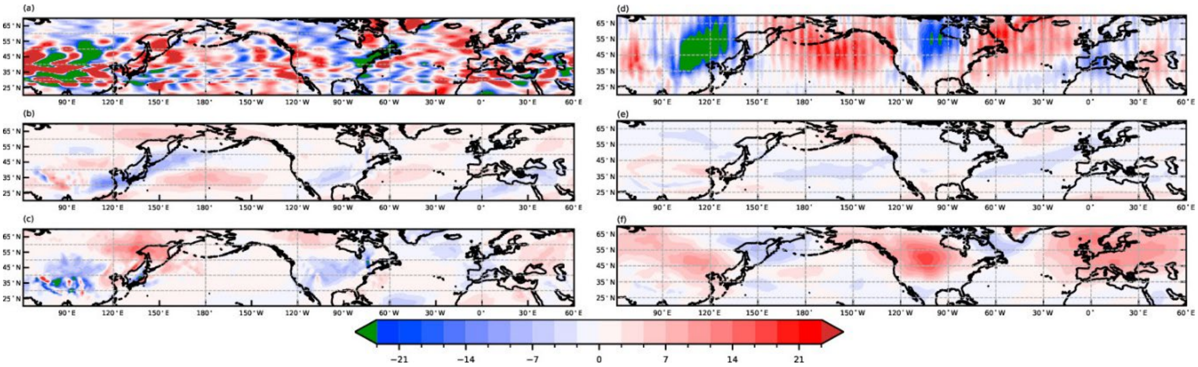

Figure 8. As in Fig. 7, but for the middle troposphere.

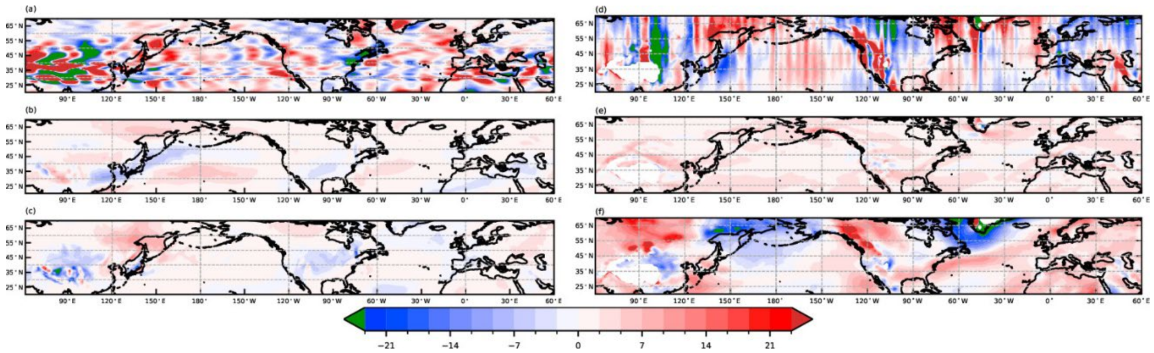

Figure 9. As in Fig. 7, but for the lower troposphere, where the flux convergence values in (a, b, c) and (d, e, f) have been multiplied by 3×10^3 and 3, respectively, to bring them within the scale used.

formulation. The only structure of note is the dominance of zonal flux divergence (convergence) in the west (east) of the North Pacific storm track (Figs. 9a and 9d). The vertical structure over the area between the northeast of the US and Greenland is noteworthy, as the vertical flux divergence in the lower to middle troposphere (for the Lagrangian results) is replaced by vertical flux convergence in the upper troposphere (Fig. 7f). Combined with the upper-tropospheric zonal wave emission over the same area shown in Fig. 7d, this vertical structure makes it definite that the source of the emission lies in the lower troposphere.

4-6 The vertical structure of diagnostics for the selected regions

To obtain a better picture of the vertical structure, for a selection of regions related to the North Atlantic and Mediterranean storm tracks, the area-average vertical profiles of the horizontal flux divergence, vertical flux divergence, and nonconservative source/sink are presented in Figs. 10a–10c for the Eulerian small-amplitude and Figs. 10d–10f for the Lagrangian finite-amplitude formulations. In the absence of a closed-form expression for the nonconservative source/sink, and given the nonlinear interaction between stationary and transient eddies (Youngblut and Sasamori, 1980; Wills and Schneider, 2015), the diagnostics are performed without attempting to partition the contributions of stationary and transient eddies. The selected regions include: the west of the North Atlantic, from 60°W to 30°W; the Mediterranean, from 30°N to 50°N, with three subareas: the western Mediterranean (from 15°W to 5°E), the central Mediterranean (from 5°E to 25°E), and the eastern Mediterranean (from 25°E to 45°E). The west of the North Atlantic region roughly corresponds to the emission area of the North Atlantic storm track. The subareas of the Mediterranean are meant to cover the zonal variation in the storm track as described in Rezaeian et al. (2016).

For the horizontal flux divergence, the main features of the small-amplitude results include upper-tropospheric divergence (convergence) over the west of the North Atlantic (the subareas of the Mediterranean) with a sign reversal at the middle to lower tropospheric levels (Fig. 10a). A similar picture emerges in the finite-amplitude results shown in Fig. 10d, which is more definite but involves much less vertical variation. All the subareas of the Mediterranean tend to act as wave reception zones, especially near 10 km pseudo-height. Below about 6 km pseudo-height, one can see a sign reversal at the central and eastern Mediterranean, turning wave-reception areas into wave emitters (Fig. 10d). For the vertical flux divergence, the west of the North Atlantic is marked by a minimum near 8 km pseudo-height, which is larger in the Lagrangian formulation (cf. Figs. 10b and 10e). The subareas of the Mediterranean behave as flux divergent in the west and flux convergent in the east for the Eulerian formulation (Fig. 10b). In contrast, the subareas of the Mediterranean have all positive maximum near 10 km pseudo-height in the finite-amplitude formulation (Fig. 10e). Additionally, there is a remarkable symmetry between the horizontal and vertical flux divergences for the finite-amplitude formulation, leading to large cancellations. The estimations of the source/sink, as shown in Figs. 9c and 9f, point to the clear advantage of the finite-amplitude formulation in providing generally smaller values with a much smoother vertical structure. While the nonconservative processes tend to primarily act as sinks of wave activity, positive values are also observed in the form of a relatively large maximum near 10 km pseudo-height in

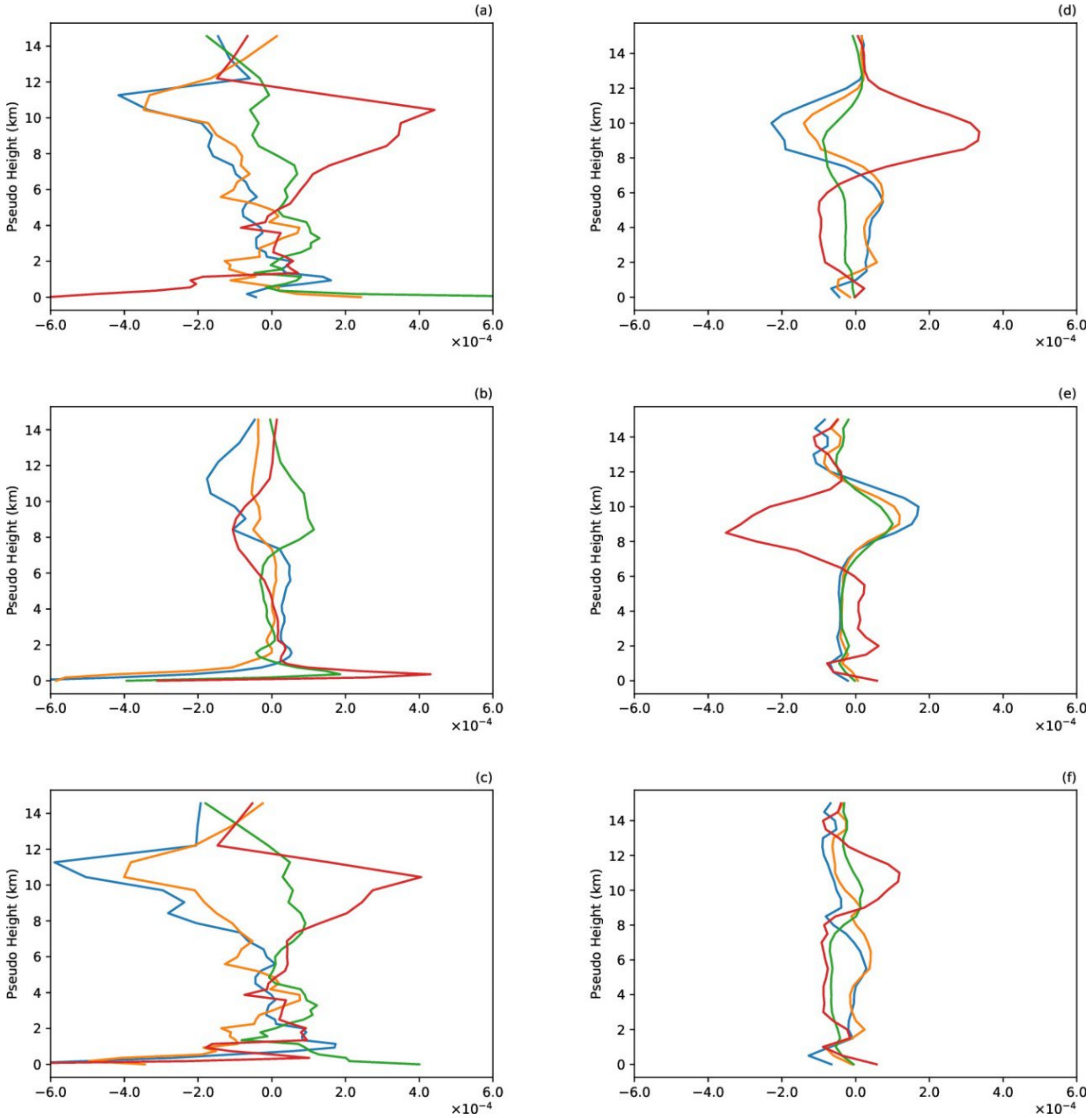

Figure 10. The vertical profiles of area-averaged (a,d) horizontal and (b,e) vertical LWA flux divergence, and (c,f) the nonconservative processes over the western North Atlantic (red), the western Mediterranean (blue), the central Mediterranean (orange), and the eastern Mediterranean (green), averaged over boreal winters (DJF) from 1979 to 2023. Results shown are for the EH formulations (a–c) and HN formulations (d–f), with units of $\mathrm{m/s^2}$.

the west of the North Atlantic, along with a few small maxima below 6 km pseudo-height in the central and western subareas of Mediterranean (Fig. 10f).

4-7 The quasigeostrophic balanced state

A potential drawback with the results given for the reanalysis data is that the derivation of the flux components in the HN formulation rests on the assumption of nondivergence of the horizontal wind field. This is evidently not the case for the horizontal wind field of the reanalysis. To address this inconsistency, a balanced state with nondivergent wind is sought, one that is compatible with the reanalysis data. To this end, the PV is inverted by setting it equal to the standard form of quasigeostrophic potential vorticity, which is formally valid for mid-latitudes. This leads to an elliptic equation for the geostrophic streamfunction (see Equation 3.2.15b in Andrews et al., 1987), which is solved in a channel from 10°N to 80°N, using the reanalysis data for the boundary conditions. The results are qualitatively in agreement with those given thus far for the reanalysis wind and temperature fields (results not shown). There are, however, certain significant quantitative differences, one example of which is related to the estimates of flux divergence and nonconservative processes, as shown in the vertical profiles of Figs. 11a–11c for the selected regions. While the horizontal and vertical flux divergences exhibit overall the same vertical variations as their counterparts in Figs. 10d–10e, the small quantitative differences lead to significant changes in the behavior of the nonconservative processes. The most dramatic of these changes is the conversion of the near-tropopause source seen in Fig. 10f into a sink in Fig. 11c. This means that the apparent near-tropopause source in the west of the North Atlantic is a result of the divergent circulation in the reanalysis wind field. It is worth noting that a similar conclusion can be made if the diagnostics are simply performed using only the geopotential height data of JRA-55 (results not shown).

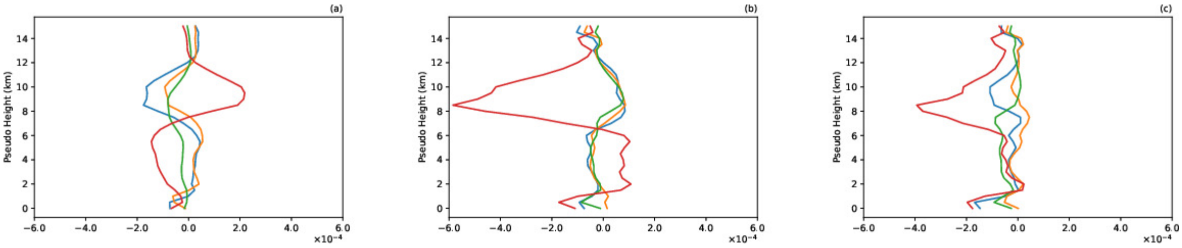

Figure 11. The vertical profiles of area-averaged (a) horizontal and (b) vertical LWA flux divergence, and (c) nonconservative processes over the western North Atlantic (red), the western Mediterranean (blue), the central Mediterranean (orange), and the eastern Mediterranean (green), averaged over boreal winters (DJF) from 1979 to 2023. Results shown are for the HN formulation using the geopotential height derived from the PV inversion. The units are m/s^2.

4-8 The diagnostics for the NECP/NCAR reanalysis

The whole diagnostics have also been provided for the $2.5^\circ \times 2.5^\circ$ NCEP/NCAR reanalysis data to examine the robustness of the main results. For the sake of brevity, only a selected set of results are presented here using the quasigeostrophic balanced state PV inversion procedure. For the near-surface vertical flux shown in Fig. 12, almost all features including the southwest–northeast oriented region of heat flux over the North Atlantic are consistent with those shown in Fig. 4 for the JRA-55. Fig. 13 presents results corresponding to those in Fig. 5 for the CZF, CMF, CHF, and the nonconservative effect (SS). Disregarding the small-scale noise seen in the results of JRA-55, mainly in the CAF (Fig. 5a),

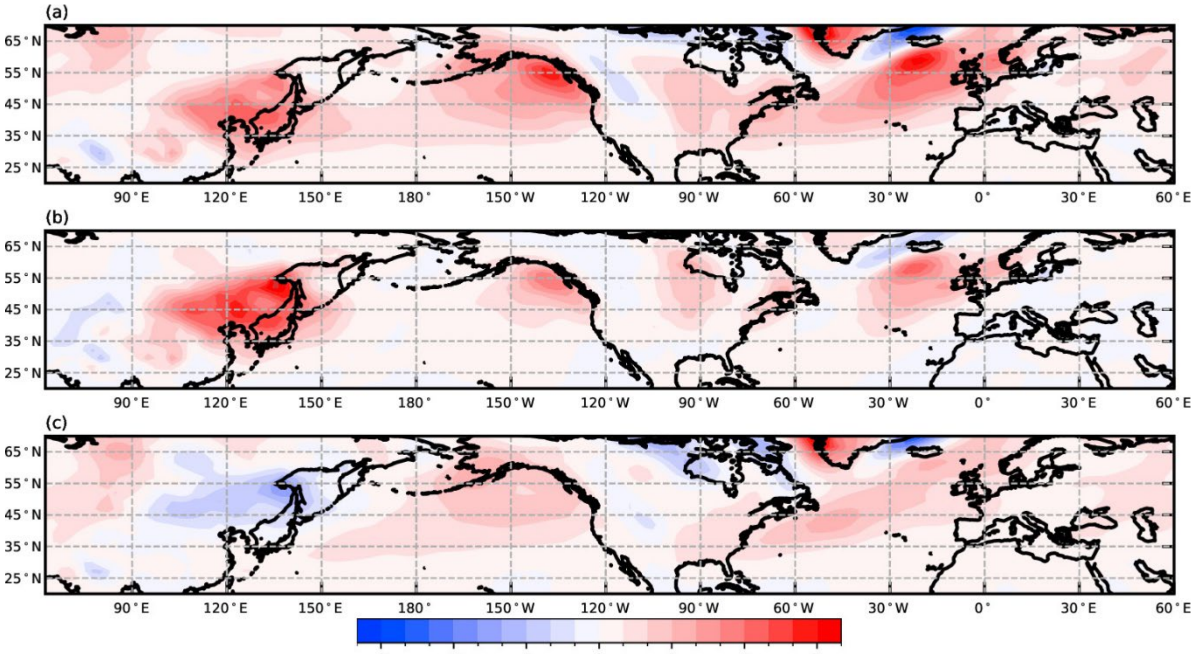

Figure 12. As Fig. 4, but for the NCEP/NCAR reanalysis data. The near-surface vertical flux of wave activity, the SF term in Eq. (10), averaged in boreal winters (DJF) from 1979 to 2023. Shown are (a) the total, (b) stationary, and (c) transient wave effects as proposed by HN17, with units of $10^{-5}\ \mathrm{m/s^2}$.

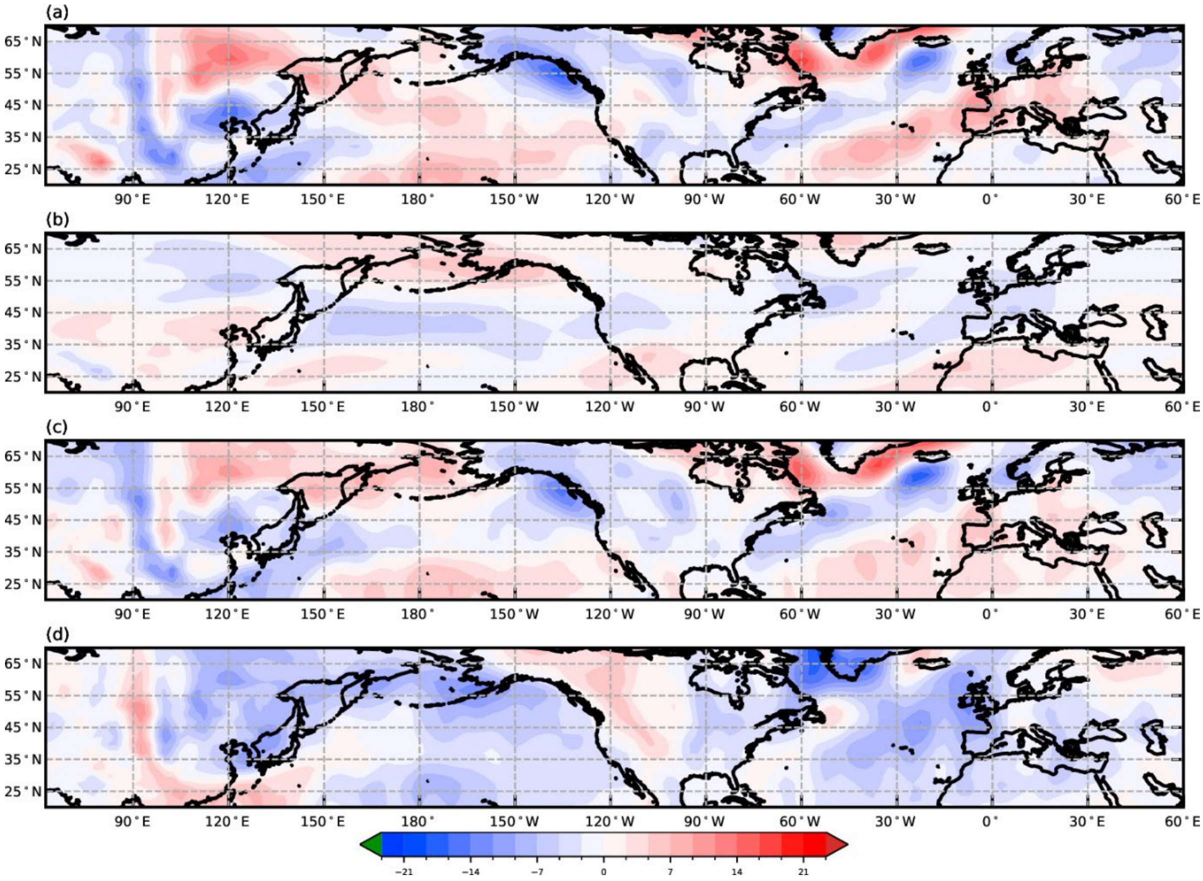

Figure 13. As Fig. 5, but for the NCEP/NCAR reanalysis data. The vertically averaged (a) CZF, (b) CMF, and (c) CHF averaged over boreal winters (DJF) from 1979 to 2023. (d) The estimate for the climatological mean of the nonconservative effect, or SS term in Eq. (10). The units are $10^{-5}\ \mathrm{m/s^2}$.

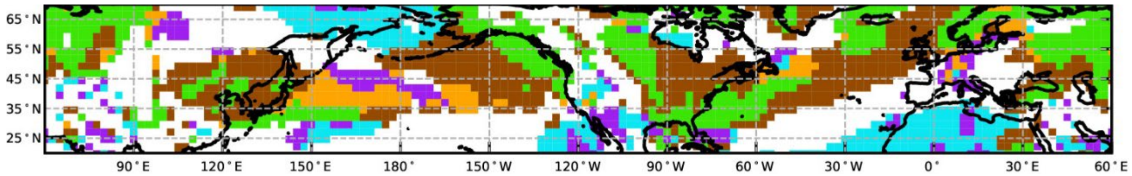

Figure 14. As Fig. 6 but for the NCEP/NCAR reanaysis data.The dominant local balance between the LWA budget terms for the average results of boreal winters (DJF) over the period 1979–2023 is as follows: The dominant balances are between the following terms: purple represents the balance between zonal and meridional flux divergence; light green represents the balance between near-surface vertical flux and zonal flux divergence; white represents the balance between zonal flux divergence and nonconservative processes; light blue represents the balance between meridional flux divergence and nonconservative processes; brown represents the balance between near-surface vertical flux and nonconservative processes; and orange represents the balance between near-surface vertical flux and meridional flux divergence. To remove small-scale noise, a low-pass spectral filter with a cutoff zonal wavenumber 30 has been applied to the advective zonal flux.

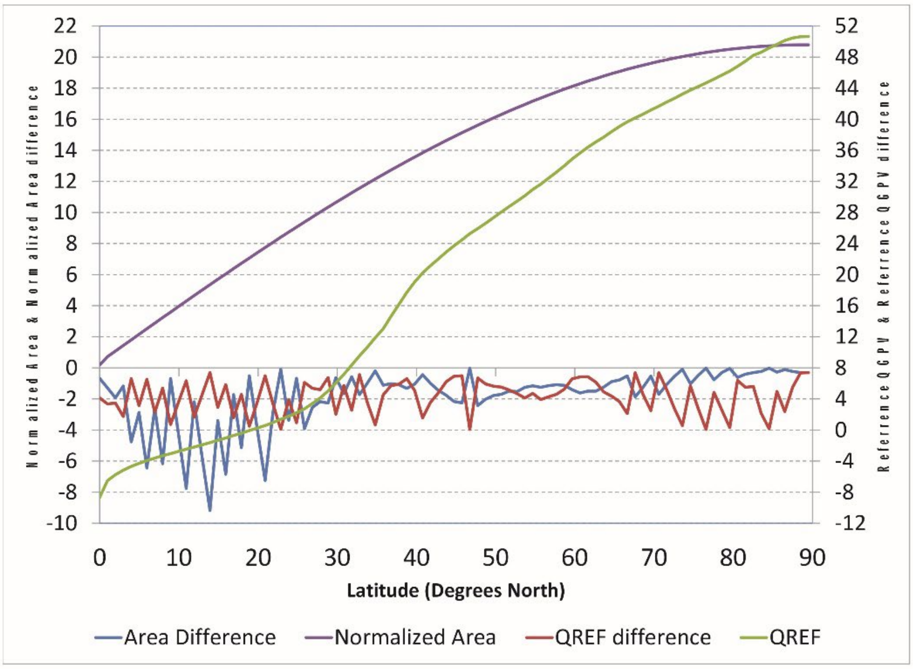

Figure 15. Comparison of the reference PV and the normalized area obtained using both uniform segmentation and the method designed in this study by exploiting all discrete PV values. The following are presented: Q_{REF} using all discrete PV values (green); Q_{REF} (unit $10^{-5}/s$) using all discrete PV values minus Q_{REF} from uniform segmentation (red); the scaled sum of areas with PV smaller than Q_{REF} ($A_{q<Q_{\mathrm{REF}}}$ with a unit of 10^3 times the area of a $1^\circ \times 1^\circ$ grid cell at the equator) using all discrete PV values (purple); and the normalized area difference (blue), which is $A_{q<Q_{\mathrm{REF}}}$ from uniform segmentation minus $A_{q<Q_{\mathrm{REF}}}$ using all discrete PV values. The units for the normalized area difference and Q_{REF} difference are one-tenth of the corresponding units for the normalized area and Q_{REF}, respectively.

there is a high-degree of agreement between the results of the two datasets. In fact, the lower resolution of the NCEP/NCAR data has helped to provide a clearer picture of the storm tracks, particularly with respect to the distribution of wave emission and wave reception regions of the oceanic storm tracks (cf. Figs. 13c and 5c). The summarization map of the dominant balance among the four terms (CZF, CMF, SF, and SS) provides the ultimate test of consistency among the reanalysis datasets. In this apsect, one can compare the summarization map of the

NCEP/NCAR data (Fig. 14) with that of the JRA-55 in Fig. 6. In brief, the results from the NCEP/NCAR data provide further evidence for characterizing the major storm tracks with a three-part structure in the column-wise wave-activity budget. The structure is composed of a strong horizontal wave emission region in the west where the dominant balance is between the near-surface vertical flux and zonal flux divergence; a weak horizontal wave emission region in the northeast with the dominant balance between the near-surface vertical flux and dissipative processes; and a strong horizontal wave reception region in the southeast, where the dominant balance is between the zonal flux convergence and dissipative processes.

5 Conclusion

Since the 1990s, with the emergence of several Rossby wave activity diagnostics, attempts have been made to determine the budget of wave activity by analyzing its related flux components–whether two- or three-dimensional–to include zonally asymmetric regional variations using reanalysis data. Among the related problems, one can refer to the vertical structure of troposphere over the North Atlantic and North Pacific storm tracks (Hoskins and Valdes, 1990), atmospheric blocking events in the lower troposphere and studying the effect of stationary waves caused by the passage of flow over high topographic regions on determining the intensity and location of observed blockings (Okajima et al., 2021), and the behavior of stationary waves under climate changes (Wills et al., 2019). Focusing on the storm tracks of the Northern Hemisphere, the current study aimed at re-evaluating the budget of wave activity using the local finite-amplitude formulation of Huang and Nakamura (2016). The validity of this formulation for finite-amplitude disturbances circumvents the ambiguity on the nature of the source/sink term in the wave-activity conservation law, a major hurdle in wave-activity budget studies. Compared to the previous study by Huang and Nakamura (2017), modifications were made to the method of extracting the Lagrangian reference state for PV, and the density-weighted vertical averaging, in order to include the entire land area in the analysis. In addition to the column budget, the distribution of flux divergence for the upper, middle and lower troposphere was examined. This was complemented by the vertical profiles of the wave-activity flux divergence and nonconservative source/sink for the selected areas related to the North Atlantic and Mediterranean storm tracks. For comparison, results were also provided for the Eulerian small-amplitude formulation of Esler and Haynes (1999). The analysis was based on computations for boreal winters spanning 45 years (1979–2023), using the JRA-55 reanalysis with 1.25° spatial and 12-hour temporal resolutions at 00 UTC, interpolated to 97 equidistant logarithmic-pressure pseudo-height levels at 500 m interval.

The results for the wave-activity budget, summarized in Fig. 5, show a dominance of balance between zonal wave propagation and nonconservative processes over land. An exception to this is observed over northeastern Eurasia and northeastern North America, upstream of the Pacific and Atlantic storm tracks, respectively. These two regions, similar to the western entrance of the oceanic storm tracks, are dominated by near-surface vertical flux, mainly balanced by eastward wave propagation (light green in Fig. 6), which extends eastward into their corresponding storm tracks. In line with our previous understanding of the wave-maker effects of mountains and warm currents in the western oceanic basins, this result aligns the emitter/receiver view of the storm tracks, as mentioned in the introduction, with earlier findings from small-amplitude theories. At the same time, this picture differs significantly from that in HN17, which indicated that the balance between near-surface vertical flux and the zonal flux divergence occurs to the east of the North Atlantic. While exhibiting overall similar distributions of dominant balance, significant differences can be distinguished between the North Pacific and North Atlantic storm tracks, particularly at their northern flanks. In the North Atlantic storm track, there is a pronounced stretched region of local balance between the near-surface source and the nonconservative processes. The more pronounced presence of meridional flux divergence at the north of the Pacific storm track is especially notable. This difference aligns well with the stronger cyclonic LWA upstream of the North Pacific storm track compared to the North Atlantic (Fig. 3a), as well as with the broader region of cyclonic wave breaking observed in Fig. 10 of Gabriel and Peters (2008) and Fig. 2a of Riviére et al. (2010), north of the North Pacific storm track. On the other hand, to the south and southeast of the North Atlantic, meridional flux divergence plays a key role in forming the dominant balance with zonal flux divergence (purple in Fig. 6) over a compact region, and with nonconservative processes (light blue in Fig. 6).

The relatively small values of the terms in the LWA conservation relation over the Mediterranean, the most active storm track region outside the two oceanic ones, exhibit a rather complicated pattern of local balances in the wintertime budget. While both nonconservative processes and zonal wave propagation play a determining role over most of the Mediterranean basin, there are areas in the central and eastern Mediterranean where the near-surface vertical flux contributes to the dominant balance. In this aspect, the Mediterranean storm track differs from the North Atlantic storm track in the absence of the near-surface vertical flux or surface baroclinicity in the dominant balance over its upstream, at the beginning of the storm track. The overall conclusion is that the Mediterranean storm track can be regarded as the downstream extension of the North Atlantic storm track from the local finite-amplitude wave-activity perspective.

Examination of the vertical variation of the flux divergence components and the nonconservative processes leads to several important results. First, when finite amplitude diagnostics are considered, there is an eastward shift in the position of the wave emission/reception regions in the upper troposphere relative to the middle troposphere. Second, while the Mediterranean region behaves mostly as the recipient of activity from the North Atlantic storm track in the upper troposphere, the distinct character of the Mediterranean storm track becomes more evident in the middle troposphere. Third, the estimates of the nonconservative processes are quite sensitive to how the reanalysis data are used to construct the wave-activity fluxes. Inconsistent use of quasigeostrophic theory by direct application of wind and temperature data from reanalysis may lead to spurious sources of wave activity, such as those observed near the tropopause to the west of the North Atlantic storm track.

As a final remark, it remains an open question whether it is possible to move beyond quasigeostrophic theory and extend the local finite-amplitude wave-activity diagnostics to more accurate balanced models with a broader domain of applicability on the sphere. Such diagnostics could provide stronger measures of Rossby-wave structure and development in the storm tracks. Another direction for research is the application of these results to climate models for both historical and future periods, in order to study the response of the storm tracks to the pressing issue of global warming.

Acknowledgements

We would like to thank the University of Tehran for its support during this research.

Appendix A: Algorithm to extract the reference state PV

As in each time step and each pressure or log-pressure level, the values of Q in the North Pole and the equator are set to the Northern Hemisphere maximum and minimum values of PV, respectively, it remains to find Q values in between. For this, two sets of areas are defined: (i) the area north of a set of latitudes given by:

$$A(\varphi) = \int_{\varphi}^{\pi/2} \int_{0}^{2\pi} a^2 \cos(\varphi')\, d\lambda\, d\varphi' \approx 6.378^2 \times 10^{12} \times 2\pi \times (1 - \sin(\varphi))' \quad \text{(A1)}$$

and (ii) the total area of grid cells with PV greater than a set of Q contours shown by dark gray color in Fig. 1 and denoted by $A(Q)$. With a knowledge of $A(\varphi)$ and $A(Q)$ values, the problem is then to find Q in terms of φ. The procedure in HN17 has been to divide the range between the hemispheric (global) maximum $q_{\max}$ and minimum $q_{\min}$ to ny_{e} uniform steps of length dq according to:

$$dq = \frac{q_{\max} - q_{\min}}{ny_{\mathrm{e}}}; \quad Q_j = q_{\min} + (j - j_{\min} + 1) \times dq, \; j = 1,2,\cdots,ny \quad \text{(A2)}$$

where $ny_{\mathrm{e}} = ny,\; j_{\min} = 1$ for the case of global, and $ny_{\mathrm{e}} = \left[\frac{ny}{2}\right] + 1, j_{\min} = \left[\frac{ny}{2}\right] + 1$ for the case of hemispheric computation. For any given latitude φ, there exist two successive $A(Q)$ values, denoted as $A(Q_{j+1})$ and $A(Q_j)$, such that

$$A(Q_{j+1}) \le A(\varphi) \le A(Q_j). \quad \text{(A3)}$$

The $Q(\varphi)$ values are then estimated through a straightforward application of linear interpolation, leading to the following expression:

$$Q(\varphi) = \frac{Q_j\big(A(\varphi) - A(Q_{j+1})\big) - Q_{j+1}\big(A(Q_j) - A(\varphi)\big)}{A(Q_j) - A(Q_{j+1})}. \quad \text{(A4)}$$

For reference, the method described above to estimate $Q(\varphi)$ values is called uniform segmentation. A modified method is designed and applied in our study. First, all discrete PV values and their corresponding cell area values are put in a 2-column table. A third column is added which holds element-wise product of the other two columns, the differential Kelvin circulation. The table is organized in ascending order of the PV values. Next, the area and circulation columns are aggregated based on the unique PV values to attain a lookup table. The two columns are then aggregated cumulatively. The area column will now contain the area of grid cells with PV values smaller than or equal to a certain occurred value. This is equivalent to the Northern Hemisphere area, excluding the dark gray region shown in Fig. 1. Another lookup table is also produced to determine the corresponding area in the south of each discrete latitude, which is equal to the Northern Hemisphere area minus the light gray region in Fig. 1. The areas in the PV and latitude tables are equal to $A(Q)$ and $A(\varphi)$, respectively. Now the area value from the latitude table is looked up in the PV table, and linear interpolation is applied between adjacent unique PV values to obtain the reference state PV with a significantly higher degree of precision and resemblance to the expected continuous form for Q_{REF}.

The net effect of applying our modified method instead of uniformly segmented PV values using (A2) is investigated in Fig. 15 for the 10 km pseudo-height level at 00 UTC 1 January 2009. The results in Fig. 15 show generally greater Q_{REF} values and its corresponding scaled area when the modified method is used. The difference in Q_{REF} is near to 4×10^{-6}/s for all latitudes. While this difference seems small even near the equator (compare the red and green curves in Fig. 15), it cannot be disregarded near to 30°N, where Q_{REF} changes sign. The normalized area difference shows a different signal, indicating that lower latitudes are more significantly affected by the uniform segmentation. Although the difference in the scaled area (as observed by comparing the blue and purple curves in Fig. 15) is small, approximately 0.2 units, and tends to zero at high latitudes, it becomes significant between 10°N and 20°N. This finding suggests that increasing the accuracy of Q_{REF} will extend the domain of validity of the LWA diagnostics further to the south. However, for the studies that are only concerned with mid-latitudes, the uniform segmentation may provide a sufficiently accurate estimation of Q_{REF}.

Appendix B: The Eulerian small-amplitude formulation

In this formulation, the flux components for the zonal $F^{(\lambda)}$, meridional $F^{(\phi)}$, and vertical $F^{(p)}$ are:

$$\begin{bmatrix} F^{(\lambda)} \\ F^{(\varphi)} \\ F^{(p)} \end{bmatrix} = \begin{bmatrix} UA \\ 0 \\ 0 \end{bmatrix} + \frac{\cos\varphi}{2} \begin{bmatrix} \frac{1}{2}(\psi' q' - v'\xi) + v'^2 - \frac{\psi' \partial v' / \partial\lambda}{a\cos\varphi} \\ -u'v' + \frac{\psi \partial u' / \partial\lambda}{a\cos\varphi} \\ \frac{f}{\partial\Theta/\partial p}\left(v'\theta' - \frac{\psi' \partial\theta' / \partial\lambda}{a\cos\varphi}\right) \end{bmatrix}, \tag{B1}$$

where ψ is the geostrophic streamfunction, and U, Θ and Q are the basic state zonal velocity, potential temperature and PV, respectively. The prime quantities are for the perturbation defined by deviation from the seasonal mean, and $A = a\cos\phi(q'^2 - (\xi\partial q'/\partial\lambda)/(a\cos\phi))/(4\partial Q/\partial\varphi)$. The variable ξ is uniquely defined by:

$$\frac{\partial\xi}{\partial\lambda} = a\cos\varphi\left(q' - \overline{q'}\right), \tag{B2}$$

where the overbar denots the zonal mean, and q' represents the perturbation PV, defined as:

$$q' = \frac{1}{a^2\cos^2\varphi}\frac{\partial^2\psi'}{\partial\lambda^2} + \frac{1}{a^2\cos\varphi}\frac{\partial}{\partial\varphi}\left(\cos\varphi\frac{\partial\psi'}{\partial\varphi}\right) + f\frac{\partial}{\partial p}\left(\frac{\theta'}{\frac{\partial\Theta}{\partial p}}\right) \cdot \tag{B3}$$

References

Andrews, D. G., Holton, J. R., and Leovy. C. B., 1987, Middle Atmosphere Dynamics: Academic Press.

Azarm, K., Mohebalhojeh, A. R., and Mirzaei, M., 2023, The changes in dynamical tropopause associated with the Euro-Atlantic and West-Asia atmospheric blocking: Dynamics of Atmospheres and Oceans, **102**, 101361.

Chang, E. K. M., Lee, S., and Swanson, K. L., 2002, Storm track dynamics: Journal of Climate, **15**, 2163–2183.

Chen, G., Lu, J., Burrows, D. A., and Leung, L. R., 2015, Local finite-amplitude wave activity as an objective diagnostic of mid-latitude extreme weather: Geophysical Research Letters, **42**(24), 10,952–10,960.

Esler, J. G., and Haynes, P. H., 1999, Baroclinic wave breaking and the internal variability of the tropospheric circulation: Journal of the Atmospheric Sciences, **56**, 4014–4031.

Esmaeli, S., Mohebalhojeh, A. R., and Mirzaei, M., 2022, Impacts of the QBO and ENSO on upper-tropospheric Rossby-wave activity associated with the North Atlantic and Mediterranean storm tracks: Quarterly Journal of the Royal Meteorological Society, **148**, 3869–3884.

Gabriel, A., and Peters, D., 2008, A diagnostic study of different types of Rossby wave breaking events in the northern extra-tropics: Journal of The Meteorological Society of Japan, **86**, 613–631.

Haynes, P. H., 1988, Forced, dissipative generalization of finite-amplitude wave-activity conservation relations for zonal and non-zonal basic flows: Journal of the Atmospheric Sciences, **45**, 2352–2362.

Hoskins, B. J., and Valdes, P. J., 1990, On the existence of storm-tracks: Journal of Atmospheric Sciences, **47**(15), 1854–1864.

Huang, C. S. Y., and Nakamura, N., 2016, Local finite-amplitude wave activity as a diagnostic of anomalous weather events: Journal of the Atmospheric Sciences, **73**(1), 211–229.

Huang, C. S. Y., and Nakamura, N., 2017, Local wave activity budgets of the wintertime Northern Hemisphere: Implication for the Pacific and Atlantic storm tracks: Geophysical Research Letters, **44**(11), 5673–5682.

Kobayashi, Sh., Ota, Y., Harada, Y., et al., 2015, The JRA-55 reanalysis: General specifications and basic characteristics: Journal of the Meteorological Society of Japan, **93**, 5–48.

Methven, J., and Berrisford, P., 2015, The slowly evolving background state of the atmosphere: Quarterly Journal of the Royal Meteorological Society, **141**, 2237–2258.

Nakamura, M., Kadota, M., and Yamane, S., 2010, Quasigeostrophic transient wave activity flux: Updated climatology and its role in polar vortex anomalies: Journal of the Atmospheric Sciences, **67**, 3164–3189.

Nakamura, N., and Huang, C. S. Y., 2018, Atmospheric blocking as a traffic jam in the jet stream: Science, **361**(6397), 42–47.

Nakamura, N., and Solomon, A., 2010, Finite-amplitude wave activity and mean flow adjustments in the atmospheric general circulation. Part I: Quasigeostrophic theory and analysis: Journal of the Atmospheric Sciences, **67**, 3967–3983.

Nakamura, N., and Zhu, D., 2010, Finite-amplitude wave activity and diffusive flux of potential vorticity in eddy-mean flow interaction: Journal of the Atmospheric Sciences, **67**(9), 2701–2716.

Neal, E., Huang, C. S. Y., and Nakamura, N., 2022, The 2021 Pacific Northwest heat wave and associated blocking: Meteorology and the role of an upstream cyclone as a diabatic source of wave activity: Geophysical Research Letters, **49**(8), e2021GL097699, https://doi.org/10.1029/2021GL097699.

Nie, Y., Zhang, Y., Zuo, J., Wang, M., Jie Wu, and Liu, Y., 2023, Dynamical processes controlling the evolution of early-summer cut-off lows in Northeast Asia: Climate Dynamics, **60**(3), 1103–1119.

Okajima, S., Nakamura, H., and Kaspi, Y., 2021, Cyclonic and anticyclonic contributions to atmospheric energetics: Scientific Reports, **11**(1), 13202.

Plumb, R. A., 1986, Three-dimensional propagation of transient quasi-geostrophic eddies and its relationship with the eddy forcing of the time-mean flow: Journal of Atmospheric Sciences, **43**(16), 1657–1678.

Rezaeian, M., Mohebalhojeh, A. R., Ahmadi-Givi, F., and Nasr-Esfahany, M., 2016, A wave-activity view of the relation between the Mediterranean storm track and the North Atlantic Oscillation in winter: Quarterly Journal of the Royal Meteorological Society, **142**, 1662–1671.

Riviére, G., Laîné, A., Lapeyre, G., Salas-Mélia, D., and Kageyama, M., 2010, Links between Rossby wave breaking and the North Atlantic Oscillation—Arctic Oscillation in present-day and last glacial maximum climate simulations: Journal of Climate, **23**, 2987–3008.

Sacha, P., Kuchar, A., Eichinger, R., Pisoft, P., Jacobi, C., and Rieder, H. E., 2021, Diverse dynamical response to orographic gravity wave drag hotspots—a zonal mean perspective: Geophysical Research Letters, **48**(13), e2021GL093305.

Scherrmann, A., Wernli, H., and Flaounas, E., 2023, The upstream-downstream mechanism of North Atlantic and Mediterranean cyclones in semi-idealized simulations: EGUsphere [preprint], https://doi.org/10.5194/egusphere-2023-2125.

Takaya, K., and Nakamura, H., 2001, A formulation of a phase-independent wave-activity flux for stationary and migratory quasigeostrophic eddies on a zonally varying basic flow: Journal of the Atmospheric Sciences, **58**(6), 608–627.

Teubler, F., Riemer, M., Polster, C., Grams, C. M., Hauser, S., and Wirth, V., 2023, Similarity and variability of blocked weather-regime dynamics in the Atlantic-European region: Weather and Climate Dynamics, **4**(2), 265–285.

Valva, C., and Nakamura, N., 2021, What controls the probability distribution of local wave activity in the midlatitudes?: Journal of Geophysical Research: Atmospheres, **126**.

Wang, M., Zhang, Y., and Lu, J., 2021, The evolution dynamical processes of Ural blocking through the lens of local finite-amplitude wave activity budget analysis: Geophysical Research Letters, **48**.

Wills, R. C. J., White, R. H., and Levine. X. J., 2019, Northern Hemisphere stationary waves in a changing climate: Current Climate Change Reports, **5**(4), 372–389.

Wills, R. C., and Schneider, T., 2015, Stationary eddies and the zonal asymmetry of net precipitation and ocean freshwater forcing: Journal of Climate, **28**(6), 5115–8842.

Youngblut, C., and Sasamori, T., 1980, The nonlinear effects of transient and stationary eddies on the winter mean circulation. Part I: Diagnostic analysis: Journal of the Atmospheric Sciences, **37**, 1944–1957.

Zhao, Y., and Liang, X. S., 2019, Causes and underlying dynamic processes of the mid-winter suppression in the North Pacific storm track: Science China Earth Sciences, **62**(5), 872–890.